Active terahertz beam steering by photo-generated graded index gratings in thin semiconductor films

T. P. Steinbusch,[1] H. K. Tyagi,[1] M.C. Schaafsma,[1] G. Georgiou,[1] and J. Gómez Rivas[1,2,*]

[1]*Center for Nanophotonics, FOM Institute AMOLF, Science Park 102, 1098 XG, Amsterdam, The Netherlands*

[2]*COBRA Research Institute, Eindhoven University of Technology, P.O. Box 513, 5600 MB Eindhoven, The Netherlands*

[*]*rivas@amolf.nl*

Abstract: We demonstrate active beam steering of terahertz radiation using a photo-excited thin layer of gallium arsenide. A constant gradient of phase discontinuity along the interface is introduced by an spatially inhomogeneous density of free charge carriers that are photo-generated in the GaAs with an optical pump. The optical pump has been spatially modulated to form the shape of a planar blazed grating. The phase gradient leads to an asymmetry between the +1 and -1 transmission diffracted orders of more than a factor two. Optimization of the grating structure can lead to an asymmetry of more than one order of magnitude. Similar to metasurfaces made of plasmonic antennas, the photo-generated grating is a planar structure that can achieve large beam steering efficiency. Moreover, the photo-generation of such structures provides a platform for active THz beam steering.

OCIS codes: (230.1150) All-optical devices; (230.1950) Diffraction gratings; (260.1960) Diffraction theory; (050.5080) Phase shift; (230.6120) Spatial light modulators.

References and links

1. N. Yu, P. Genevet, M. A. Kats, F. Aieta, J. P. Tetienne, F. Capasso, and Z. Gaburro, "Light propagation with phase discontinuities: generalized laws of reflection and refraction," Science **334,** 333 (2011).
2. A. V. Kildishev, A. Boltasseva, and V. M. Shalaev, "Planar photonics with metasurfaces," Science **339,** 1232009 (2013).
3. H. J. Visser, *Array and Phased Array Antenna Basics* (Wiley, 2005).
4. J. Sun, A. Yaacobi, E. S. Hosseini and M. R. Watts, "Large-scale nanophotonic phased array," Nature **493,** 195–199 (2013).
5. S. Larouche and D. R. Smith, "Reconciliation of generalized refraction with diffraction theory," Opt. Lett. **37,** 2391 (2012).
6. F. Aieta, P. Genevet, N. Yu, M. A. Kats, Z. Gaburro, and F. Capasso, "Out-of-plane reflection and refraction of light by anisotropic optical antenna metasurfaces with phase discontinuities," Nano Lett. **12**, 1702 (2012).
7. B. Walther, C. Helgert, C. Rockstuhl, F. Setzpfandt, F. Eilenberger, E. B. Kley, F. Lederer, A. Tnnermann, and T. Pertsch, "Spatial and spectral light shaping with metamaterials," Adv. Mat. **24**, 6300 (2012).
8. S. Sun, K. Y. Yang, C. M. Wang, T. K. Juan,W. T. Chen,C. Y. Liao, Q. He, S. Xiao, W. T. Kung, G. Y. Guo, L. Zhou, and D. P. Tsai, "High-efficiency broadband anomalous reflection by gradient metasurfaces," Nano Lett. **12**, 6223 (2012).
9. M. F. Farahani and H. Mosallaei, "Birrefringent reflectarray metasurface for beam enginnering in infrared," Opt. Lett. **38**, 462 (2013).

#217467 - $15.00 USD Received 21 Jul 2014; revised 14 Oct 2014; accepted 14 Oct 2014; published 20 Oct 2014

10. N. Grady, J. E. Heyes, D. R. Chowdhury, Y. Zeng, M. T. Reiten, A. K. Azad, A. J. Taylor, D. A. R. Dalvit, and H. T. Chen, "Terahertz metamaterials for linear polarization conversion and anomalous refraction," Science **340**, 1304 (2013).
11. A. Pors and S. I. Bozhevolnyi, "Plasmonic metasurfaces for efficient phase control in reflection," Opt. Express **21**, 27438 (2013).
12. X. Zhang, Z. Tian, W. Yue, J. Gu, S. Zhang, J. Han, and W. Zhang, "Broadband terahertz wave deflection based on C-shape complex metamaterials with phase discontinuities," Adv. Mat. **25**, 4567 (2013).
13. Z. Wei, Y. Cao, X. Su, Z. Gong, Y. Long, and H. Li, "Highly efficient beam steering with a transparent metasurface," Opt. Express **21**, 10739 (2013).
14. T. Roy, A. E. Nikolaenko, and E. T. F. Rogers, "A meta-diffraction-grating for visible light," J. Opt. **15**, 085101 (2013).
15. M. D. Goldflam, T. Driscoll, D. Barnas, O. Khatib, M. Royal, N. M. Jokerst, D. R. Smith, B. J. Kim, G. Seo, H. T. Kim, and D. N. Basov, "Two-dimensional reconfigurable gradient index memory metasurface," Appl. Phys. Lett. **102**, 224103 (2013).
16. D. Hu, X. Wang, S. Feng, J. Ye, W. Sun, Q. Kan, P. J. Klar, and Y. Zhang, "Ultrathin terahertz planar elements," Adv. Opt. Mat. **1**, 186 (2013).
17. Y. Huang, Q. Zhao, S. K. Kalyoncu, R. Torun, Y. Lu, F. Capolino, and O. Boyraz, "Phase-gradient gap-plasmon metasurface based blazed grating for real time dispersive imaging," Appl. Phys. Lett. **104**, 161106 (2014).
18. G. Georgiou, H. K. Tyagi, P. Mulder, G. J. Bauhuis, J. J. Schermer, and J. Gómez Rivas, "Photo-generated THz antennas," Sci. Rep. **4,** 3584 (2014).
19. N. Kanda, K. Konishi, and M. Kuwata-Gonokami, "All-photoinduced terahertz optical activity," Opt. Lett. **39**, 3274 (2014).
20. T. Okada and K. Tanaka, "Photo-designed terahertz devices," Sci. Rep. **1**, 121 (2011).
21. I. Chatzakis, P. Tassin, L. Luo, N. Shen, L. Zhang, J. Wang, T. Koschny, and C. M. Soukoulis, "One- and two-dimensional photo-imprinted diffraction gratings for manipulating terahertz waves," Appl. Phys. Lett. **103,** 043101 (2013).
22. S. Busch, B. Scherger, M. Scheller, and M. Koch, "Optically controlled terahertz beam steering and imaging," Opt. Lett. **37,** 1391 (2012).
23. Z. Xie, X. Wang, J. Ye, S. Feng, W. Sun, T. Akalin, and Y. Zhang, "Spatial terahertz modulator," Sci. Rep. **3,** 3347 (2013).
24. M. Schall and P. Jepsen, "Photoexcited GaAs surfaces studied by transient terahertz time-domain spectroscopy," Opt. Lett. **25,** 13 (2000).
25. P. G. Huggard, J. A. Cluff, G. P. Moore, C. J. Shaw, S. R. Andrews, S. R. Keiding, E. H. Linfield, and D. A. Ritchie, "Drude conductivity of highly doped GaAs at terahertz frequencies," J. Appl. Phys. **87,** 2382 (2000).
26. C. Hilsum, "Simple empirical relationship between mobility and carrier concentration," Electron. Lett. **10,** 259 (1974).
27. P. Yeh, *Optical Waves in Layered Media* (Wiley, 1988).
28. M. C. Troparevsky, A. S. Sabau, A. R. Lupini, and Z. Zhang, "Transfer-matrix formalism for the calculation of optical response in multilayer systems: from coherent to incoherent interference," Opt. Express **18,** 24715 (2010).
29. D. Paget, F. Cadiz, A. C. H. Rowe, F. Moreau, S. Arscott, and E. Peytavit, "Imaging ambipolar diffusion of photocarriers in GaAs thin films," J. Appl. Phys. **111,** 123720 (2012).
30. N. D. Arora, J. R. Hauser, and D. J. Roulston, "Electron and hole mobilities in silicon as a function of concentration and temperature," IEEE Trans. Electron Dev. **29,** 292 (1982).
31. S. Adachi, *Handbook on Physical Properties of Semiconductors* (Kluwer, 2004).
32. S. C. Howells and L. A. Schlie, "Transient terahertz reflection spectroscopy of undoped InSb from 0.1 to 1.1 THz," Appl. Phys. Lett. **69,** 550 (1996).
33. K. K. Chen and J. K. Furdyna, "Temperature dependence of intrinsic carrier concentration in InSb: direct determination by helicon interferometry," J. Appl. Phys. **43,** 1825 (1972).
34. Gentec-EO, https://www.gentec-eo.com/downloads/technical-documentation (Winston Cone Accesory).
35. Gentec-EO, https://www.gentec-eo.com/products/thz-detectors/THZ-B (THz-B Detectors).
36. L. Zou, W. Withayachumnankul, C. M. Shah, A. Mitchell, M. Bhaskaran, S. Sriram, and C. Fumeaux, "Dielectric resonator nanoantennas at visible frequencies," Opt. Express **21,** 1344 (2013).

1. Introduction

Control over the propagation direction of electromagnetic waves is commonly achieved with optical components such as lenses, gratings and mirrors. Recently, the concept of metasurfaces was proposed by Yu and co-workers [1] as a mean to achieve this control at mid-IR frequencies and extended to the near infrared by Kildishev and co-workers [2]. Metasurfaces are planar

#217467 - $15.00 USD Received 21 Jul 2014; revised 14 Oct 2014; accepted 14 Oct 2014; published 20 Oct 2014

optical components, which contain arrays of subwavelength plasmonic scatterers of varying shape, resonant frequencies and/or orientation. Light scattered by the subwavelength structures acquires a different phase and the far-field interference of these scattered waves gives rise to beaming in defined directions or to more complex wave front shapes. This concept shares some similarities with antenna phased arrays in which antenna elements emit radiation into the far field with a defined phase relation relative to other elements to achieve beaming [3, 4]. The directional beam steering by metasurfaces has been described in the context of generalized laws of refraction and reflection in which a constant gradient of phase discontinuity along the interface is introduced by the subwavelength scatterers [1]. The phase discontinuity increases by 2π over a length-scale that defines the period of a planar grating. The generalized laws of reflection and refraction are a simple way of describing complicated wave propagation through interfaces using ray optics; However, they are limited to scatterers with equal scattering amplitudes separated by a distance much smaller than the wavelength, which ensures planar reflected and transmitted wavefronts. Larouche and Smith employed a more general description using wave diffraction theory to explain the anomalous reflection and refraction [5]. Using diffraction theory it can be shown that the generalized laws are equivalent to the diffraction of blazed gratings in which light transmitted at different positions acquires a different phase delay due to the variation of the thickness of the grooves. A difference between metasurfaces and blazed gratings is that the former are surfaces in which phase delays are introduced by planar scatterers, while blazed gratings are in general non-planar structures. Therefore, possibility of realizing planar optical components by means of metasurfaces has motivated intensive research on this field [6–17].

In this manuscript we demonstrate active THz beam steering with planar photo-generated blazed gratings. This is achieved on a thin gallium arsenide (GaAs) layer by using a graded illumination profile over the period of the grating. This graded illumination produces a spatially dependent free-carrier density in the layer that increases linearly with the illumination fluence. An incident THz pulse, time-delayed with respect to the optical pump, experiences a phase delay that depends on the free-carrier density. An important element for the photo-generation of the blazed gratings is a spatial light modulator. These devices allows to change the illumination pattern and provides an unprecedented degree of freedom for achieving active steering of the THz beam. Photo-generated antennas [18] and chiral structures [19] have been recently demonstrated using structured illumination of semiconductors. Also photo-generated gratings [20, 21] and controlled THz diffraction has been demonstrated [22, 23]. However, none of the previous works has shown an asymmetric scattering or diffraction as we do here, nor relates the results to the rapidly emerging field of metasurfaces.

Using the graded photo-excitation of GaAs, we show an asymmetry of more than a factor two between the +1 and -1 diffracted orders of broadband THz radiation. We also discuss how this asymmetry can be improved to more than one order of magnitude by using different semiconductors at higher frequencies. Our designs suggest a steering efficiency that is similar to that demonstrated with metasurfaces at IR frequencies, with the advantage of a much simpler design and, more importantly, the active control of THz beam steering introduced by the optical pump.

2. Sample description and characterization

For the experiments we used a single crystalline layer of GaAs grown by metalorganic chemical vapor deposition and with a thickness of 1 μm. After growth, the GaAs layer is transferred and bonded to a SiO_2 substrate as described in [[18]]. The bonding layer is a 40 μm mercapto-ester based polymer layer.

When the GaAs layer is optically pumped with photons that exceed the bandgap energy, free

#217467 - $15.00 USD Received 21 Jul 2014; revised 14 Oct 2014; accepted 14 Oct 2014; published 20 Oct 2014

carriers are generated. The permittivity $\bar{\varepsilon} = \varepsilon' + i\varepsilon''$ as a function of the carrier density N can be described by the Drude model for free charge carriers [24, 25]. The Drude permittivity is given by

$$\bar{\varepsilon} = \varepsilon_\infty - \frac{\omega_p^2}{\omega + 1/\tau^2}\left(\frac{1}{i\omega\tau} + 1\right), \tag{1}$$

where τ is the average electron-electron collision time and ω_p is the plasma frequency. $\varepsilon_\infty = 12.85$ denotes the GaAs permittivity at high frequencies and $\omega = 2\pi\nu$ is the angular frequency of the electromagnetic radiation. The average scattering time $\tau = \frac{m^*\mu_\mathrm{m}}{e}$ is related to the carrier mobility μ_m, the elementary charge e and the effective mass of the electrons in GaAs $m^* = 0.063 m_\mathrm{e}$, where m_e is the electron mass. For the thin film GaAs sample used in this manuscript we use a mobility of $\mu_\mathrm{m} = 0.5\ \mathrm{m^2V^{-1}s^{-1}}$, which is extracted from fitting THz transmission measurements through the sample using the Drude values for the permittivity of GaAs with μ_m as a free fitting parameter. This value deviates from the mobility in bulk GaAs ($\mu_\mathrm{m,bulk} = 0.94\ \mathrm{m^2V^{-1}s^{-1}}$ for undoped GaAs at $T = 300$ K [26]), probably due to a residual doping of the GaAs and to surface scattering at the boundaries of the thin layer. The permittivity $\bar{\varepsilon}$ is directly related to the complex refractive index, $\bar{n}$, by

$$\bar{n} = n + i\kappa = \sqrt{\bar{\varepsilon}}. \tag{2}$$

Because the plasma frequency is related to the carrier density N by $\omega_p = \sqrt{\frac{Ne^2}{m^*\varepsilon_0}}$ the above formulas allow us to calculate the refractive index as a function of N.

Figure 1(a) shows the complex refractive index of GaAs as a function of the carrier density calculated using the Drude model at $\nu = 1$ THz. For $N = 10^{15}\ \mathrm{cm^{-3}}$ the layer has a refractive index $n = 3.5$ and $\kappa \approx 0$. For this N the layer has a dielectric behavior as indicated by the positive value of the real part of the permittivity ε' displayed in the inset of Fig. 1(a). The real component of the refractive index decreases to $n = 2.4$ at $N = 1.8\times10^{16}\ \mathrm{cm^{-3}}$. For this carrier density the layer becomes metallic ($\mathrm{Re}(\varepsilon') < 0$). For higher values of N, n rapidly increases as it is expected for a layer with a Drude-like behavior. The imaginary component of the refractive index κ increases monotonously for increasing N.

Using the transfer matrix method [27, 28] and the complex refractive index of GaAs as it is obtained from the Drude model, we can determine the amplitude and phase of THz waves transmitted through the GaAs layer as a function of N. For these calculations we consider a three layer system surrounded by air. The three layers are the SiO_2 substrate (thickness $d = 1$ mm, $n = 2.0$, $\kappa = 0$), the mercapto-ester based bonding polymer ($d = 40\ \mu$m, $n = 1.6$, $\kappa = 0$) and the 1 μm thick layer of GaAs. The calculated normalized transmission amplitude T/T_0 and phase shift $\Delta\phi = \phi - \phi_0$ at $\nu = 1$ THz are shown in Fig. 1(b). The reference used to normalize the transmission and phase is obtained by using the same three layers but with an intrinsic number of carriers for the GaAs ($n = 3.56, \kappa = 0$) instead of the (optically-)doped GaAs.

The transmission amplitude of the THz field through the layer decreases with increasing N. This is attributed to an increased reflection and absorption as the layer becomes metallic for $N > 1.8\times10^{16}\ \mathrm{cm^{-3}}$. The phase shift difference decreases from 0 up to a value of -0.25π for a carrier concentration of $N = 1.5\times10^{18}\ \mathrm{cm^{-3}}$. This behavior of the phase shift is caused by the interplay of two effects [24]. First, a change in the optical path length $l = \int n(s)ds$, where $n(s)$ denotes the index of refraction along the optical path s, is expected to cause the phase shift

$$\Delta\phi = \frac{2\pi\nu}{c}\Delta l, \tag{3}$$

where c denotes the speed of light in vacuum. The optical path length changes due to a change in n and because of internal reflections.

#217467 - $15.00 USD Received 21 Jul 2014; revised 14 Oct 2014; accepted 14 Oct 2014; published 20 Oct 2014

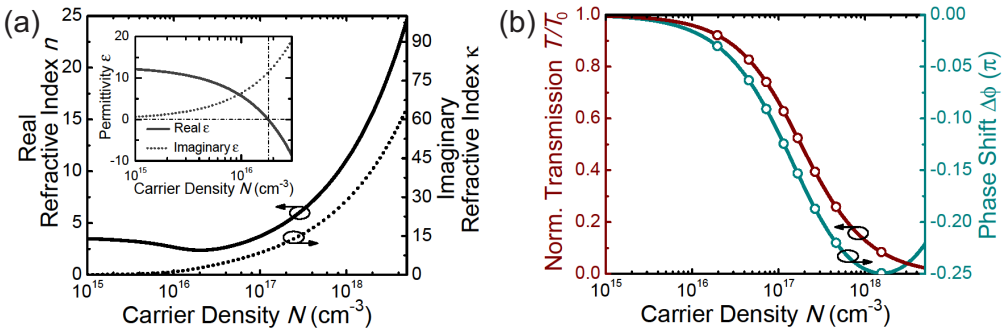

Fig. 1. (a) Real (solid) and imaginary (dotted) components of the refractive index of GaAs at $\nu = 1$ THz as a function of the carrier density, N, calculated using the Drude model. The inset shows the complex permittivity as a function of N. (b) Transmission amplitude at $\nu = 1$ THz through a GaAs layer with a 1μm thickness calculated as a function of the carrier density and normalized to the transmission through an intrinsic GaAs layer (red circles and curve). The cyan circles and curve correspond to the phase shift difference between the transmission through the GaAs layer with carrier density N and the transmission through the intrinsic GaAs layer.

The second contribution to the phase shift arises from the transmission at the interfaces and it is described by the Fresnel coefficients. In order to illustrate this contribution, we consider a plane wave E_1 with an amplitude A_1 in a non-absorbing medium 1 ($n_1 > 0$, $\kappa_1 = 0$) traveling in the x direction. The field in an absorbing medium 2 ($n_2 > 0$, $\kappa_2 > 0$) upon transmission at normal incidence can be written as

$$E_2 = \bar{t}_{1,2} E_1 = \bar{t}_{1,2} A_1 \exp\left(ik_1 x - i\omega_1 t\right), \tag{4}$$

where $k_1 = \frac{2\pi}{\lambda}$ denotes the wave number, ω_1 is the angular frequency of the wave in medium 1, and $\bar{t}_{1,2}$ is the complex Fresnel coefficient given by

$$\bar{t}_{1,2} = |t_{1,2}| \exp\left(\phi_{1,2}\right) = \frac{n_1}{n_1 + (n_2 + i\kappa_2)}. \tag{5}$$

The phase shift upon transmission at the interface is given by

$$\Delta\phi_{1,2} = -\tan^{-1}\left(\frac{\kappa_2}{n_1 + n_2}\right), \tag{6}$$

and the phase shift of the EM wave transmitted into the second layer is always negative if medium 2 has a non-zero κ_2. The above derivation can be extended to a system that contains a layer with refractive index $n_2, \kappa_2 > 0$ in between two layers with $n_1 > 1$ and $\kappa_1 = 0$ by taking the product of the complex transmission coefficients at the two interfaces $\bar{t}_{1,2}$ and $\bar{t}_{2,3}$. The total phase shift due to the transmission though the interfaces in such system is

$$\Delta\phi_{1,3} = \Delta\phi_{1,2} + \Delta\phi_{2,3} = -\tan^{-1}\left(\frac{(n_2 - n_1 + \kappa_2^2)\kappa_2}{(n_1 + n_2)(n_2^2 + n_1 n_2 + \kappa_2^2) + n_1\kappa_2^2}\right). \tag{7}$$

Although Eq. (7) is an approximation that ignores multiple reflections, it illustrates that the phase shift due to the interfaces is negative if the central layer is absorptive and $n_2 > n_1$, as it is the case for our multilayered sample.

#217467 - $15.00 USD Received 21 Jul 2014; revised 14 Oct 2014; accepted 14 Oct 2014; published 20 Oct 2014

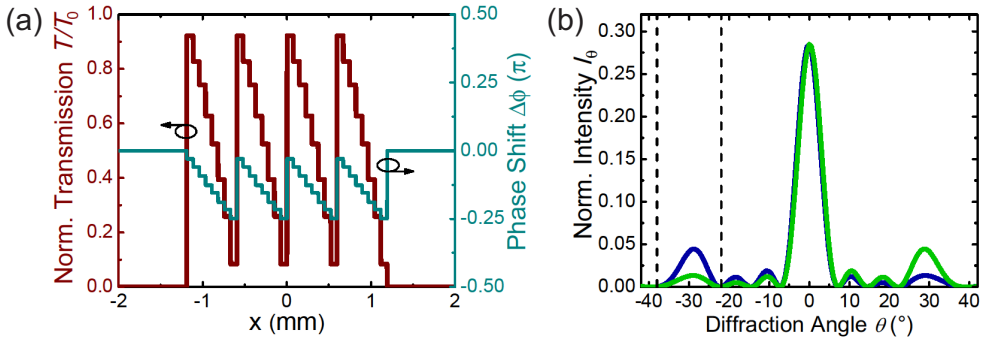

Fig. 2. (a) Blazed grating with 4 grating periods and a grating constant $\Gamma = 600$ μm. One grating period consists of the 8 carrier densities indicated by the circles in Fig. 1(b), N decreases from right to left in each period. (b) Calculated far-field intensity pattern at $\nu = 1$ THz of the blazed grating with a decreasing carrier density from right to left (blue) and from left to right (green) in each period. The intensity is normalized by the transmission through a fully transparent window with the dimension of 4 grating periods and zero transmission outside. The vertical dashed lines indicate the angular range of interest for the experiment.

3. Experimental results

3.1. Photo-generation of blazed gratings

Planar blazed gratings were generated by local photo-excitation of free carriers in the GaAs layer. The layer was excited using a 100 fs pump pulse with a central wavelength of $\lambda = 800$ nm (1.55 eV) and a repetition rate of 1 KHz. The carrier recombination time in the sample was experimentally determined to be $\tau_r \sim 450$ ps. This time is much shorter than the time between two consecutive pump pulses and hence the GaAs layer is always in its dielectric state when the pump pulse arrives.

The linearly polarized 800 nm pump beam was spatially modulated by a computer-controlled spatial light modulator (SLM) with a pixel-size of 8×8 μm^2 and a resolution of 1920×1200 pixels. Each pixel can rotate the polarization vector from 0° to 90° in a continuous way. With an analyzer it is thus possible to control the intensity reflected by each pixel [18]. Using this technique we can actively change the free carrier concentration in spatial regions comparable to the pixel-size of the SLM in the GaAs sample. The contrast in the pump fluence given by the two extreme polarization states is limited by the SLM and it is ~2 orders of magnitude. In our experiments the carrier concentrations in the GaAs layer could be changed between $N = 2 \times 10^{16}$ cm^{-3} and 1.5×10^{18} cm^{-3}.

The normalized transmission amplitude and phase shift calculated from the transfer-matrix method can be used to design a blazed grating with 8 regions of increasing carrier density in each grating period. These carrier concentrations are indicated in Fig. 1(b) by circles and are chosen such that 8 equidistant phase steps are achieved. The calculated complex transmission function of the designed blazed grating with a grating constant $\Gamma = 600$ μm is shown in Fig. 2(a). For our experiments four grating periods were chosen due to the finite size of the THz beam at the sample plane, which is similar to 4Γ. In Fig. 2(a) N increases from left to right in each grating period. This increase produces a reduction of the transmission and a linear decrease of the phase shift.

Diffraction theory can be used to calculate the diffraction pattern for the spatially varying THz amplitude and phase of Fig. 2(a). The far-field intensity pattern $I(\theta)$ of a grating structure can be determined by calculating the Fourier transform of the complex transmission function

#217467 - $15.00 USD Received 21 Jul 2014; revised 14 Oct 2014; accepted 14 Oct 2014; published 20 Oct 2014

$\bar{T}(x)$ of the structure that causes the diffraction

$$I(\theta) = \mathfrak{F}[\bar{T}(x)]^2 = \mathfrak{F}[T(x) \cdot \exp(i\phi(x))]^2 \ . \tag{8}$$

The blue curve in Fig. 2(b) shows the far field intensity pattern I_θ of the blazed grating calculated using Eq. (8). The green curve is the far-field intensity pattern of the complementary grating, i.e., a blazed grating with the same grating constant and N decreasing from left to right for each grating period. Besides the central peak, which represents the zeroth order diffraction, the +1 and -1 diffracted orders at 30° and -30° are visible. The linear change of phase shift produces a pronounced asymmetry in the intensity between these orders.

Diffraction theory predicts that the beam steering efficiency depends on three factors. First, the phase shift $\Delta\phi(x)$ achieved in each grating period. When the phase shift is less than 2π there is light scattered into other diffraction orders and the beam steering efficiency decreases. Second, the transmission amplitude $T(x)$ throughout the grating. If this is less than unity there is light absorbed or reflected by the grating structure and hence the efficiency of the grating decreases. Third, the number of grating periods in the structure. The grating orders are sharper when the grating consists of a larger number of grating periods. The small amount of periods in the grating shown in Fig. 2(a), together with the reduction in the transmission and the limited phase shift, are the reasons for the relatively small change of the diffracted intensities depending on the blazing. In Section 3.3 we describe other structures that can significantly improve the steering efficiency.

3.2. THz diffraction measurements

Figure 3(a) shows images of the blazed gratings photo-generated in our setup using the SLM. These images were taken by replacing the GaAs sample in the setup by a CCD camera. The color scale represents the illumination fluence. The upper panel displays the grating with carrier density N increasing in each period from left to right, while the lower panel corresponds to the grating with decreasing N. Cuts through the images along the horizontal dashed lines are shown in the central panel of Fig. 3(a) by the blue and green curves for the increasing and decreasing N, respectively. The right axis in this panel is the estimated photo-generated carrier density obtained from the illumination fluence.

In order to measure the beam steering by the photo-generated blazed gratings we used THz pulses generated by a THz time-domain spectrometer (THz-TDS) [18]. These pulses probed the photo-generated grating at a time delay with the optical pulse of 10 ps $<< \tau_r$. The intensity spectrum of the THz pulse is shown in Fig. 4. The carrier diffusion length in the sample over this time window is $\sim$140 nm [29]. This is much shorter than the characteristic length scale in the experiment, i.e. the pixel-size of the SLM. The THz pulse is weakly focussed at the sample position with a full width half maximum (FWHM) of ≈ 2.5 mm.

Since the configuration of the THz-TDS was quite rigid and designed to measure only the zeroth-order transmission ($\theta = 0^\circ$), we used a pyroelectric detector to detect the diffracted orders of the photo-generated blazed gratings. In order to enhance the signal-to-noise ratio, a Winston cone was placed in front of the detector to collect the radiation over a larger solid angle of 0.56 sr. The Winston cone is very sensitive to the angle of incidence, e.g. for an angle of incidence that deviates 4° from its axis the detected signal by the detector is reduced by a factor of 2. Therefore, the cone is also used as a spatial filter to reduce the scattered THz radiation detected by the pyroelectric detector at angles other than the diffraction angle. In the experiments the pyroelectric detector was placed at a distance of 72 mm behind the sample at $\theta = -30^\circ$ and 30° with respect to the normal of the sample surface. The pyroelectric detector could be only used for relative intensity measurements because there is no calibration available for the absorption efficiency of the device at frequencies below 0.75 THz. This absorption efficiency

#217467 - $15.00 USD Received 21 Jul 2014; revised 14 Oct 2014; accepted 14 Oct 2014; published 20 Oct 2014

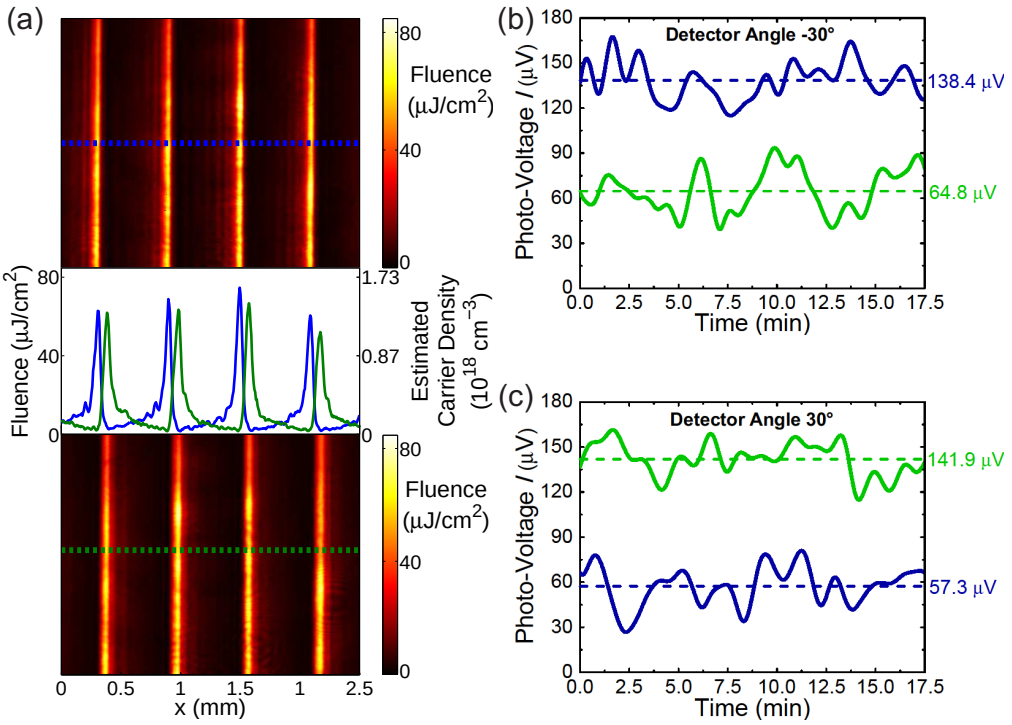

Fig. 3. (a) CCD camera images of the 800 nm pump beam at the sample position. The pump beam is spatially modulated by the SLM in the shape of a blazed grating with $\Gamma = 600\ \mu$m with a carrier tail to the left (top) and to the right (bottom). The central panel shows cuts through both gratings along the horizontal dotted lines. (b) Output of the pyroelectric detector at a position of $\theta = -30^\circ$ with respect to the normal to the surface of the sample. The green curve corresponds to the signal measured when the blazed grating has a decreasing carrier density from left to right; The blue curve corresponds to a blazed grating with a carrier density decreasing from right to left. (c) The same as in (b) but at a detector angle of $\theta = 30^\circ$ with respect to the normal to the surface of the sample.

is $\sim 10\%$ for frequencies between 0.75 - 1 THz and increases rapidly for higher frequencies. The photo-voltage in the pyroelectric detector was detected by a phase-demodulation technique using a lock-in amplifier with the signal modulated at 5 Hz.

The signal from the pyroelectric detector is shown in Figs. 3(b) and 3(c) measured for $\theta = -30^\circ$ and $\theta = 30^\circ$, respectively, and for the two blazed gratings. The photo-voltage is measured for 17.5 minutes. In this time window several noise oscillations are measured and, hence, the mean value of the signal, indicated by the dashed lines in Figs. 3(b) and 3(c), can be determined. We observe a pronounced difference in the mean values, favoring the left steering grating at $\theta = -30^\circ$ and the right steering grating at $\theta = 30^\circ$. The ratios $R = I_{\text{left}}/I_{\text{right}}$ between the mean values at $\theta = \pm 30^\circ$ are $R_{-30^\circ} = 2.14 \pm 0.21$ and $R_{30^\circ} = 0.40 \pm 0.04$. The uncertainties on these ratios are determined by conducting a dark photo-voltage measurement with the THz beam blocked. This measurement is used to filter the noise in the signal. After this filtering the variance of the signal in the time-domain is used to estimate the error σ on each single photo-voltage measurement. Due to the long integration time of the lock-in amplifier ($\tau_{\text{lock-in}} = 20$ s with a filter slope of 24 dB/Oct) not all the data points shown in the curves of Figs. 3(b) and 3 (c) are uncorrelated. In total there are 9 fully uncorrelated data points of the photo-voltage in

#217467 - $15.00 USD Received 21 Jul 2014; revised 14 Oct 2014; accepted 14 Oct 2014; published 20 Oct 2014

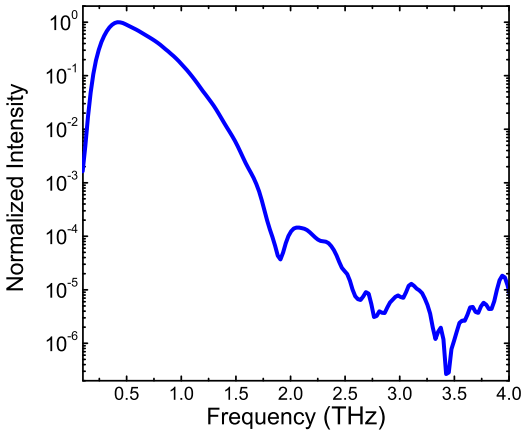

Fig. 4. Intensity spectrum of the THz probe pulse. The maximum intensity is normalized to 1.

each data set. We can treat these measurements as independent, all with an error σ. From this we can determine the standard error on the mean value of I, which is given by $\sigma_E = \frac{\sigma}{\sqrt{9}}$. The errors on R are calculated through standard error-propagation.

To further investigate the beam steering properties of the blazed gratings, a new set of measurements was conducted in which the pyroelectric detector was kept fixed at $\theta = -30^\circ$. The photo-voltage was measured for 19 left and right steering gratings with 3 periods and grating constants varying between $\Gamma = 391$ and 1174 μm. The 3 grating periods for $\Gamma = 800$ μm correspond to a length similar to the FWHM of the THz beam. For each measurement the mean value was extracted and the ratio between the mean values of the left and right steering gratings was calculated. The results are shown in Fig. 5. The experimental data show a maximum in the intensity ratio R_{-30° and an optimum in the steering peak for $\Gamma = 600$ μm.

The black curve in Fig. 5 is calculated using diffraction theory for the different grating constants. The diffracted intensity for each grating was calculated in an interval of $\pm 8^\circ$ around

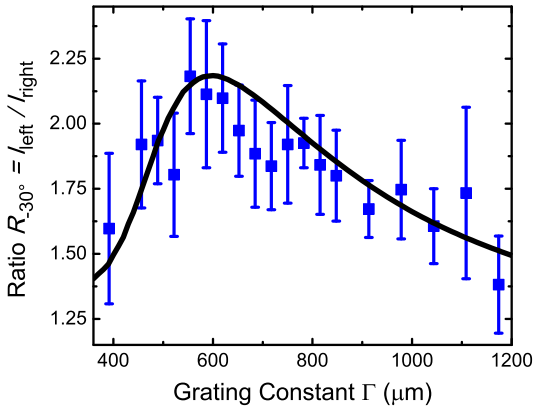

Fig. 5. Ratio between the diffracted THz intensities by the left and the right steering blazed gratings measured at $\theta = -30^\circ$ for 19 different grating constants. The blue squares are measurements and the black curve are calculations using diffraction theory.

#217467 - $15.00 USD Received 21 Jul 2014; revised 14 Oct 2014; accepted 14 Oct 2014; published 20 Oct 2014

30° and -30° and weighted by the angular response of the Winston cone [34], the frequency responsivity of the pyroelectric detector [35], and the spectrum of the generated THz radiation. The ratio between the calculated intensities at 30° and -30° was determined considering the three grating periods for each Γ. The simple diffraction model describes reasonably well qualitatively and quantitatively the measurements within the error bars. Therefore, we apply it in the next section to explore further possibilities to improve the steering efficiency.

3.3. Maximization of the beam steering

The beam steering efficiency can be increased by using a layer of semiconductor that induces a larger phase shift in the transmitted THz radiation. To investigate the effect of the semiconductor material on the steering efficiency, we have calculated the phase shift at 1 THz induced by a layer with a thickness of 1 μm and arbitrary values of n and k. The results are depicted in the contour plot of Fig. 6(a) in which the color scale indicates the phase shift $\Delta\phi_{\text{air}} = \phi - \phi_{\text{air}}$ with respect to a similar layer of air.

Superimposed to the color plot in Fig. 6(a) are three curves corresponding to the complex refractive index of GaAs, silicon (Si) and indium antimonide (InSb) for different carrier concentrations. The various ranges of N are illustrated by the different colors forming each curve (see the legend of the figure). These curves are calculated using the Drude model (Eqs. (1)-(2)). For Si we use $m^* = 0.98m_e$, $\varepsilon_\infty = 11.7$ and [30]

$$\mu_{\text{m,Si}} = \frac{1}{1000}\left[52.2 + \frac{1364.8}{1+\left(N/(1.295\times10^{17})\right)^{0.891}} - \frac{43.4}{1+\left(3.43\times10^{20}/N\right)^2}\right] \text{ m}^2\text{V}^{-1}\text{s}^{-1},$$

while for InSb we use $m^* = 0.0153m_e$, $\varepsilon_\infty = 15.68$ and [31]

$$\mu_{\text{m,InSb}} = \frac{18.03}{1+\left(N/(3\times10^{17})^{0.68}\right)} \text{ m}^2\text{V}^{-1}\text{s}^{-1}.$$

In the case of InSb, we consider a temperature of 200 K. At this temperature the intrinsic carrier concentration is $\sim 7\times10^{14}$ cm^{-3}, leading to dielectric behavior at the THz frequencies of interest [32, 33]. Figure 6(b) shows the calculated phase shift as a function of N, hence these are cuts along the (n,κ)-curves of Fig. 6(a). Within the carrier concentration range that we can reach with our experimental setup, InSb induces the largest phase shift on the transmitted THz radiation. The normalized transmission amplitude is displayed in Fig. 6(c) as a function of N. The semiconducting layers become opaque as N increases and the layer transits from dielectric to metallic behavior. From Fig. 6 we expect that using an InSb layer will increase the beam steering efficiency.

As we show next, using THz radiation with a higher frequency will improve significantly the beam steering efficiency. Figure 7 illustrates the calculation of beam steering using the Drude model, transfer-matrix method and diffraction theory for EM radiation at $\nu = 3$ THz and a 1 μm thick layer of InSb. Figure 7(a) shows the calculated normalized transmission amplitude T/T_0 and phase shift $\Delta\phi$ with respect to intrinsic InSb as a function of the carrier density. The transmission amplitude initially shows a slight increase for increasing N. This is due to a small decrease of the real part of the refractive index n for these N. For N larger than 2.8×10^{16} cm^{-3} the sample becomes metallic and the transmission amplitude decreases. The phase shift curve is shifted to larger N with respect to the case of 1 THz and a larger $\Delta\phi$ can be achieved due to the frequency dependence of Eq. (3).

Figure 7(b) shows a blazed grating design with the values of N indicated by the open circles of Fig. 7(a). As in the case of GaAs, this range of values can be achieved through illumination of the sample with a SLM. At $\nu = 3$ THz the grating constant Γ must be 3 times shorter than

#217467 - $15.00 USD Received 21 Jul 2014; revised 14 Oct 2014; accepted 14 Oct 2014; published 20 Oct 2014

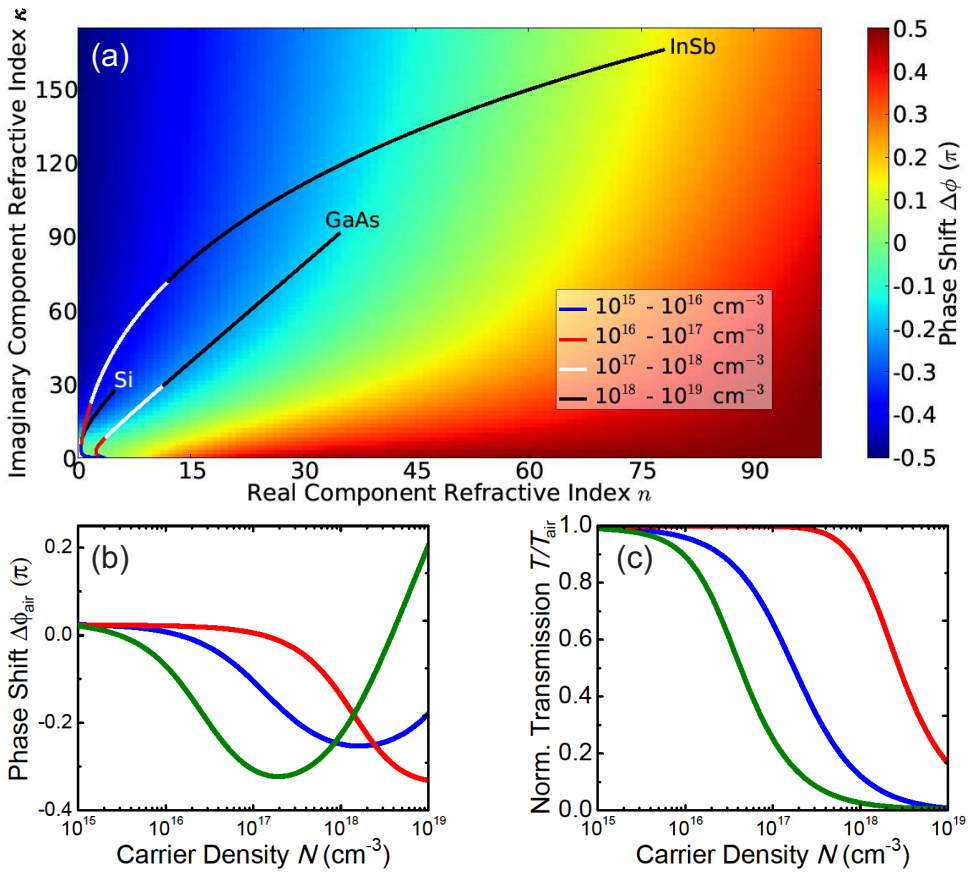

Fig. 6. (a) Phase shift difference (colorscale) between a transmitted wave of frequency $\nu =$ 1 THz through a 1 μm thick layer with complex index of refraction given by the axis and a transmitted wave through a layer of air of equal thickness. The (n,κ)-curves for GaAs, InSb and Si are calculated using the Drude model and plotted with the solid curves. Different carrier concentration ranges are indicated with different colors as described by the legend. (b) Phase shift with respect to a layer of air as a function of the carrier concentration through a 1 μm layer of GaAs (blue), InSb (green) and Si (red) at $\nu = 1$ THz. (c) Normalized transmission amplitude with respect to air as a function of the carrier concentration through a 1 μm layer of GaAs (blue), InSb (green) and Si (red) at $\nu = 1$ THz.

for $\nu = 1$ THz to obtain the first diffraction order at the same angle. Because of this reduction in Γ, it is possible to increase the number of periods that fit within the size of the THz beam. Hence, we use 12 grating periods with $\Gamma = 200$ μm to calculate the diffraction pattern. Fourier transforming the complex transmission function using Eq. (8) results in Fig. 7(c). Because of the larger number of grating periods, the diffracted orders are much narrower than the ones calculated for 1 THz in Fig. 1. Also, because of the larger phase shift induced by each grating period on the THz radiation, the beam steering efficiency increases. Integration of the intensity over the diffraction orders gives more than one order of magnitude asymmetry between the +1 and -1 diffracted orders. The calculated intensity ratios between the +1 and -1 order are in this case $R_{-30} = 13.85$ and $R_{30} = 0.07$.

The calculated difference between the zeroth and first orders is similar to that demonstrated

#217467 - $15.00 USD Received 21 Jul 2014; revised 14 Oct 2014; accepted 14 Oct 2014; published 20 Oct 2014

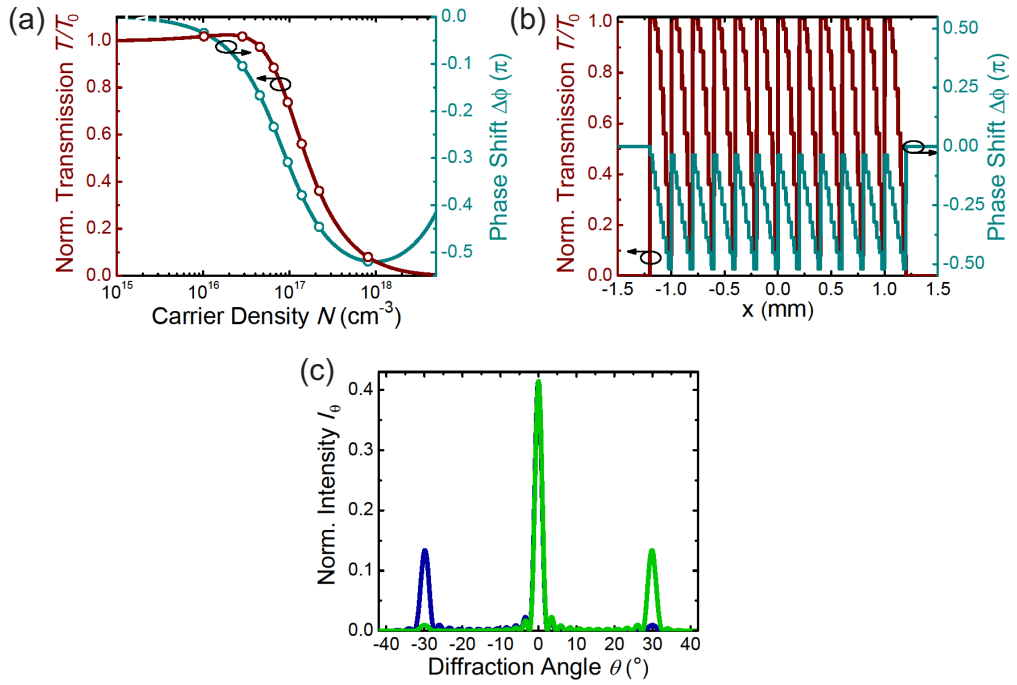

Fig. 7. (a) Calculated normalized transmission (red) and phase shift (cyan) with respect to a layer of intrinsic InSb at $\nu = 3$ THz as a function of N. (b) Blazed grating with 12 grating periods and a grating constant $\Gamma = 200$ μm. One grating period consists of the carrier densities indicated by the circles in (a). (c) Calculated far-field intensity pattern at $\nu = 3$ THz of the left (blue) and right (green) steering blazed gratings. The transmission is normalized by the transmission through a transparent window with the dimensions of the grating and zero transmission outside.

in beam steering experiments using metasurfaces [1, 36]. These experiments generally rely on the resonant properties of the structures to change the phase of the radiation at the interface. In the seminal work of Yu and co-workers, they authors used subwavelength v-shaped gold nano-antennas with changing length and angle between the two arms to change the phase of the scattered infrared light at $\lambda = 8$ μm [1]. In that work, the measured maximum relative intensity between the ordinary (zeroth order) and the anomalous (diffracted order) refraction is a factor $\sim$3 for unpolarized light at normal incidence. The fabrication of these metasurfaces is challenging due to the dimensions of the resonating structures, smaller than the wavelength of the radiation. In contrast to this, the photo-generated blazed refractive index gratings discussed here do not have these fabrication challenges and, in addition, they enable the active steering of the radiation by simply changing the illumination pattern and intensity of the semiconductor with the SLM. Therefore, photo-generated blazed gratings provide a valuable alternative for THz beam steering. We note, however, the differences between metasurfaces and photo-generated gratings in terms of the limited phase shift attainable in the last and the variable transmitted/reflected amplitudes determined by the material properties and specially N.

4. Conclusions

In conclusion, we have demonstrated the active control over the intensity of THz radiation that is diffracted into different orders by a planar blazed refractive index grating. The blazed

#217467 - $15.00 USD Received 21 Jul 2014; revised 14 Oct 2014; accepted 14 Oct 2014; published 20 Oct 2014

profile was achieved by photo-exciting free charge carriers in a thin layer of GaAs using a computer-controlled spatial light modulator. The measurements are explained using diffraction theory and considering a constant gradient of phase discontinuity along the interface. Photo-induced blazed gratings are planar structures that enable beam steering without the need of resonant subwavelength structures as in the case of metasurfaces. Ratios of intensities between the +1 and -1 diffracted orders of more than one order of magnitude can be achieved using high mobility semiconductors such as InSb.

Acknowledgments

The authors would like to acknowledge P. Mulder, G. J. Bauhuis and J. J. Schermer for the sample fabrication. This work has been supported by the ERC through grant no 259727 THZ-PLASMON and by the Netherlands Foundation for Fundamental Research on Matter (FOM) and the Netherlands Organization for Scientific Research (NWO).